Role of poroelasticity during the early postseismic deformation of the 2010 Maule megathrust earthquake

Carlos Peña[1], Sabrina Metzger[2], Oliver Heidbach[1], Jonathan R Bedford[3], Bodo Bookhagen[4], Marcos Moreno[5], Oncken Onno[6], and Fabrice Cotton[7]

[1]Helmholtz Centre Potsdam German Research Centre for Geosciences
[2]Helmholtz-Zentrum, Deutsches GeoForschungsZentrum Potsdam
[3]Deutsches GeoForschungsZentrum
[4]University of Potsdam
[5]Universidad de Concepción
[6]GeoForschungsZentrum Potsdam
[7]GFZ

November 24, 2022

Posted on 24 Nov 2022 — CC-BY 4.0 — https://doi.org/10.1002/essoar.10510987.1 — This a preprint and has not been peer reviewed. Data may be preliminary.

Abstract

Megathrust earthquakes impose changes of differential stress and pore pressure in the lithosphere-asthenosphere system that are transiently relaxed during the postseismic period primarily due to afterslip, viscoelastic and poroelastic processes. Especially during the early postseismic phase, however, the relative contribution of these processes to the observed surface deformation is unclear. To investigate this, we use geodetic data collected in the first 48 days following the 2010 Maule earthquake and a poro-viscoelastic forward model combined with an afterslip inversion. This model approach fits the geodetic data 14% better than a pure elastic model. Particularly near the region of maximum coseismic slip, the predicted surface poroelastic uplift pattern explains well the observations. If poroelasticity is neglected, the spatial afterslip distribution is locally altered by up to ±40%. Moreover, we find that shallow crustal aftershocks mostly occur in regions of increased postseismic pore-pressure changes, indicating that both processes might be mechanically coupled

Role of poroelasticity during the early postseismic deformation of the 2010 Maule megathrust earthquake

Carlos Peña[1, 2], Sabrina Metzger[1], Oliver Heidbach[1,3], Jonathan Bedford[1], Bodo Bookhagen[2], Marcos Moreno[4], Onno Oncken[1,5], and Fabrice Cotton[1,2]

[1] Helmholtz Centre Potsdam, GFZ German Research Centre for Geosciences, Potsdam, Germany

[2] Institute of Geosciences, University of Potsdam, Germany

[3] Institute of Applied Geosciences, Technical University Berlin, Germany

[4] Departamento de Geofísica, University of Concepción, Chile

[5] Department of Earth Sciences, Freie Universität Berlin, Berlin, Germany

Corresponding author: carlosp@gfz-potsdam.de

Key points

- A poro-viscoelastic deformation model improves the geodetic data misfit by 14% compared to an elastic model that only accounts for afterslip
- Poroelastic deformation mainly produces surface uplift and landward displacement patterns on the coastal forearc region
- Neglecting poroelastic effects may locally alter the afterslip amplitude by up to ±40% near the region of maximum coseismic slip

Key words: Chilean subduction zone, poroelasticity, power-law rheology, afterslip inversion, InSAR, GNSS

Abstract

Megathrust earthquakes impose changes of differential stress and pore pressure in the lithosphere-asthenosphere system that are transiently relaxed during the postseismic period primarily due to afterslip, viscoelastic and poroelastic processes. Especially during the early postseismic phase, however, the relative contribution of these processes to the observed surface deformation is unclear. To investigate this, we use geodetic data collected in the first 48 days following the 2010 Maule earthquake and a poro-viscoelastic forward model combined with an afterslip inversion. This model approach fits the geodetic data 14% better than a pure elastic model. Particularly near the region of maximum coseismic slip, the predicted surface poroelastic uplift pattern explains well the observations. If poroelasticity is neglected, the spatial afterslip distribution is locally altered by up to ±40%. Moreover, we find that shallow crustal aftershocks mostly occur in regions of increased postseismic pore-pressure changes, indicating that both processes might be mechanically coupled.

Plain Language Summary

Large earthquakes modify the state of stress and pore pressure in the upper crust and mantle. These changes induce stress relaxation processes and pore pressure diffusion in the postseismic phase. The two main stress relaxation processes are postseismic slip along the rupture plane of the earthquake and viscoelastic deformation in the rock volume. These processes decay with time, but can sustain over several years or decades, respectively. The other process that results in volumetric crustal deformation is poroelasticity due to pore pressure diffusion, which has not been investigated in detail. Using postseismic surface displacement data acquired by radar satellites after the 2010 Maule earthquake, we show that poroelastic deformation may considerably affect the vertical component of the observed geodetic signal during the first months. Poroelastic deformation also has an impact on the estimation of the postseismic slip, which in turn affects the energy stored at the fault plane that is available for the next event. In addition, shallow aftershocks within the continental crust show a good, positive spatial correlation with regions of increased postseismic pore-pressure changes, suggesting they are linked. These findings are thus important to assess the potential seismic hazard of the segment.

1. Introduction

In the aftermath of large earthquakes, the Earth surface displays time-dependent deformation patterns on different spatiotemporal scales that may last several of years or decades due to the relaxation of coseismically imposed stress and pore pressure changes in the lithosphere-asthenosphere system (e.g., Hergert and Heidbach, 2006; Hughes et al., 2010; Wang et al., 2012, and references therein). These relaxation processes are aseismic postseismic slip on the fault interface (afterslip), poroelastic processes in the upper crust, and viscoelastic relaxation in the lower crust and upper mantle (e.g., Barbot, 2018; Hughes et al., 2010; Peña et al., 2020; Sun and Wang, 2015). Afterslip distributions can be used as a proxy to gain valuable insights into the mechanical behavior of the fault interface and to quantify the remaining slip budget (Avouac, 2015, and references therein). To do so, it is compulsory to decipher the relative contribution of each postseismic process to the surface deformation. In particular, the contribution of poroelastic processes is not fully understood.

In the long-term (years to decades) and at larger spatial scales (100s of km) it is widely accepted that afterslip and viscoelastic relaxation prevail (e.g. Peña et al., 2020; 2021; Barbot, 2018; Sun et al., 2014; Wang et al., 2012). Conversely, poroelastic processes seem to contribute primarily in the early postseismic phase (days to months), especially in the near field close to the area of high coseismic slip. Here, the contribution of poroelastic processes to the surface deformation has been shown to be up to 30% compared to those due to linear viscoelastic relaxation (e.g., Hu et al., 2014; Hughes et al., 2010; Masterlark et al, 2001). However, previous studies often neglect both poroelastic and viscoelastic relaxation, assuming that afterslip is the dominant process and that the crust and upper mantle respond in a purely elastic fashion (e.g., Aguirre et al., 2019; Rolandone et al., 2018; Tsang et al., 2019). Recently McCormack et al. (2020) and Yang et al.

(2022) investigated the poroelastic effects on afterslip inversions during the first ~1.5 months following the 2012 M_w 7.8 Nicoya, Costa Rica, and 2015 M_w 8.3 Illapel, Chile, earthquakes, using Global Navigation Satellite System (GNSS) data. They show that the resulting amplitude of afterslip may be affected by more than ±50% in regions of ~40 × 40 km^2 when neglecting poroelasticity. Yet, their models ignore viscoelastic relaxation. For the same 2015 Illapel event and similar postseismic 3D GNSS data, Guo et al. (2019) find that linear viscoelastic effects may increase and reduce the resulting inverted afterslip at shallower and deeper segments, respectively, but they do not consider the potential effect of poroelastic and non-linear viscoelastic processes. Hence, the relative contributions of postseismic processes to the early postseismic phase at subduction zones are still elusive.

The postseismic deformation associated with the 2010 M_w 8.8 Maule earthquake in central-southern Chile (Figure 1) has been studied extensively using afterslip only (e.g., Aguirre et al., 2019; Bedford et al., 2013), combining afterslip and linear viscoelastic relaxation (e.g., Klein et al., 2016; Bedford et al., 2016), and afterslip and non-linear viscoelastic relaxation (Peña et al., 2019; 2020; Weiss et al., 2019). In this work, we investigate for the first time the relative contribution of afterslip, poroelastic and non-linear viscoelastic processes of the early postseismic deformation of the 2010 Maule earthquake. We use a model approach that combines a 4D forward model of poroelastic and non-linear viscoelastic relaxation with an afterslip inversion. We use displacements observed by continuous 3D GNSS sites and Interferometric Synthetic-Aperture Radar (InSAR) during the first 48 days after the main shock. We find that particularly in the near field poroelastic processes significantly affect the afterslip estimates and could explain the observed postseismic uplift signal.

2. Geodetic observations

3D GNSS displacements time-series are obtained using the processing strategy explained in Bedford et al. (2020). Data are retrieved in the International Terrestrial Reference Frame (ITRF) 2014 and then rotated to a Stable South American reference frame. Seasonal signals and offsets caused by aftershocks are removed using sparse linear regression of a modified trajectory model (Bedford and Bevis, 2018). We do not remove the interseismic component because it is negligible compared to the surface deformation in the first 48 days. We select only stations that account for at least 38 daily solutions, resulting in 20 GNSS sites (Figure 1). We linearly interpolate gaps in the time series up to 10 days assuming linear behavior (e.g., Bedford et al., 2013; Moreno et al., 2012).

To increase the spatial coverage, we complete the GNSS data with InSAR line-of-sight (LOS) displacement. We used an image pair of the L-Band (23.6 cm wavelength) ALOS PALSAR satellite mission from the Japanese Space Agency. The scenes were acquired on descending pass in ScanSAR wide-beam mode on the 1st of March (Scene ID: ALPSRS218444350) and 16th of April (ALPSRS225154350), thus spanning day 2 to 48 following the earthquake. The differential interferogram was created after co-registration and burst synchronization using the GAMMA software (Wegmüller and Werner, 1997; Werner et al., 2011). To increase the coherence, we multi-looked the original interferogram 3, resp., 16 times in range/azimuth to a spatial resolution of 30/50 m. We removed the topographic phase using a 90 m digital elevation model from the Shuttle Radar Topography Mission (Farr et al., 2007). We further improved the signal-to-noise ratio with an adaptive phase filter (Goldstein & Werner, 1998) and unwrapped the phase using Minimum Cost Flow (Costantini, 1998). The geocoded LOS displacements were quad-tree subsampled (Welstead, 1999; Jónsson et al., 2002) to a total number of 586 data samples using the Kite software (Isken et al., 2017) from the open-source seismology toolbox Pyrocko (Heimann et al., 2017). Uncertainties were estimated using the full variance-covariance matrix (Sudhaus and Jónsson, 2009). Finally, we removed the long-wavelength orbital signal by minimizing the misfit between the LOS InSAR displacements (averaged on a 15×15 km^2 window at each GNSS position) and the GNSS data (collapsed into LOS) using a linear ramp (e.g., Cavalié et al., 2013). The GNSS and deramped InSAR data are then used for the afterslip inversion.

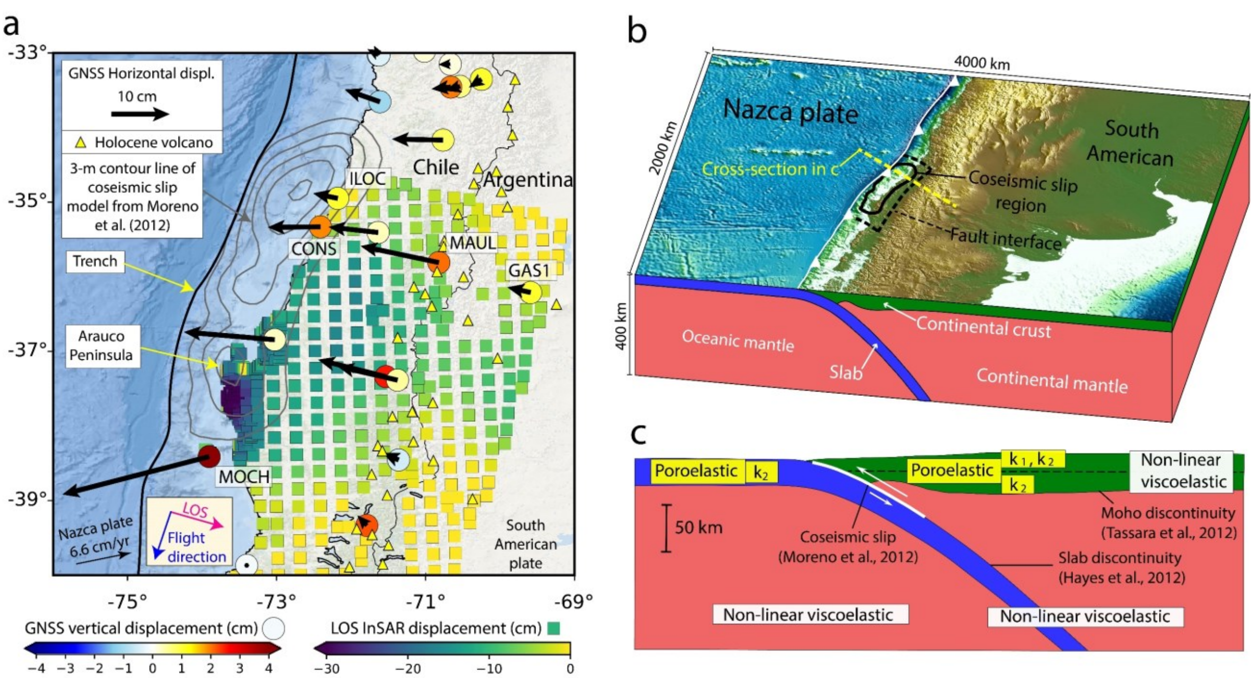

Figure 1. a) Cumulative postseismic InSAR and GNSS surface displacements between the days 2 and 48 after the 2010 Maule M_w 8.8 earthquake. Negative LOS values indicate relative motion away from the satellite. b) 3D view and c) cross-section of the model illustrating layers and rheology with k as permeability described in section 3.

3. Model setup

We use the model workflow of Peña et al. (2020), where the postseismic surface displacements produced by 4D forward simulation are first subtracted from the geodetic data. The remaining signal is then inverted for afterslip. Here, we extend the forward model part of Peña et al. (2020) by adding poroelasticity to the model (Figure 1c).

We simulate the postseismic non-linear rock viscous deformation under high-temperature and high-pressure conditions as:

$$\dot{\varepsilon}_{cr} = A\sigma^n exp\left(\frac{-Q}{RT}\right) \tag{1}$$

where $\dot{\varepsilon}_{cr}$ is the creep strain rate, A is a pre-exponent parameter, σ the differential stress, n the stress exponent, Q the activation energy for creep, R the gas constant and T the absolute temperature (e.g., Hirth & Kohlstedt, 2003). The poroelastic response is simulated following the approach of Wang (2000), where the constitute equations of mass conservation and Darcy's law describe the coupled displacement (u) and pore-fluid pressure (p) in Cartesian coordinates (x) expressed in index notation as follows:

$$G\nabla^2 u_i + \frac{G}{(1-2\nu)}\frac{\partial^2 u_k}{\partial x_i \partial x_k} = \alpha\frac{\partial p}{\partial x_i} \tag{2}$$

$$\alpha\frac{\partial \varepsilon_{kk}}{\partial t} + S_\epsilon\frac{\partial p}{\partial t} = \frac{k}{\mu_f}\nabla^2 p \tag{3}$$

Here, G and ν are the shear modulus and the drained Poisson ratio, respectively, α is the Biot-Willis coefficient, t the elapsed time since the main shock, S_ϵ the constrained storage coefficient, $\varepsilon_{kk} = \partial u_k/\partial x_k$ is the volumetric strain, k the intrinsic permeability and μ_f the pore-fluid viscosity (Wang, 2000). The subscript i represents the three orthogonal spatial directions, while the subscript k denotes the summation over these three components (Hughes et al., 2010).

The onset of the poroelastic and viscoelastic postseismic deformation is driven by the coseismically induced response (e.g., Hughes et al., 2010; Masterlark et al., 2001; MacCormarck et al., 2020). We prescribe the coseismic slip model of Moreno et al. (2012) as displacement boundary conditions on the fault interface (Peña et al., 2020). The lateral and bottom model boundaries are free to displace parallel to their faces. We also apply stress-free and no-flow boundary conditions in the surface layer (e.g., Hughes et al., 2010; Tung and Masterlark, 2018). The resulting numerical problem is solved with the commercial finite element software ABAQUS™, version 6.14.

Given the high uncertainty of rock permeability, temperature, and viscous creep parameters, we consider end-member scenarios for the crust and upper mantle (Figure 1c; Tables S1 and S2). We consider two scenarios with lower and upper bounds of permeability of 1×10^{-16} m^2 and 1×10^{-14} m^2 for the continental crust in the upper 15 km (Völker et al., 2011), while we set a permeability of 1×10^{-16} m^2 for the lower crust, as obtained from crustal-scale studies in Chile (e.g., Husen and Kissling, 2001; Koerner et al., 2004) and other regions (e.g., Ingebritsen and Manning, 2010). We adopt quartzite and diabase creep parameters for the continental crust, and wet olivine with 0.01 and 0.005 percent of water for the upper mantle (e.g., Hirth & Kohlstedt, 2003; Peña et al., 2020). We do not further explore rock property changes for the oceanic crust and mantle due to the lack of offshore measurements to constrain our results. We thus set a permeability of 1×10^{-16} m^2 for the oceanic plate (Fisher, 1998), and assign diabase and wet olivine with 0.005 percent of water creep parameters for the slab and oceanic mantle, respectively (Peña et al., 2020).

During the afterslip inversion, we determine the relative weights of InSAR and GNSS data sets by identifying the optimal misfit value between the observed and modelled surface displacement that does not substantially vary the misfit of each individual data set (e.g., Cavalié et al., 2013; Melgar et al., 2017). We find that the relative weights for GNSS and InSAR are 1 and 0.6, respectively (Figure S2). This agrees with the tendency of lowering the InSAR data weight when including GNSS and InSAR along with land-leveling (Moreno et al., 2012) and strong motion data (Melgar et al., 2017) that found relative weights of about 0.5 and 0.3 for GNSS and InSAR data, respectively. Furthermore, we neglect the postseismic processes coupling as it does not change the results beyond the GNSS data uncertainty (Figure S3).

4. Model results compared to geodetic observations

All GNSS horizontal postseismic displacements show trench-ward motion (Figure 1). The maximum cumulative surface displacement reaches 24.5 cm at station MOCH, while the maximum cumulative InSAR LOS displacement is observed at the Arauco Peninsula with 32.5 cm. The volcanic arc region also exhibits significant long-wavelength deformation, reaching ~15 cm and ~2 cm in the horizontal and vertical components at the station MAUL, respectively. Along the coastline, the observations exhibit strong vertical variations. The northern part subsides by up to 1 cm, while the two GNSS sites (ILOC and CONS) near the region of maximum coseismic slip yield uplift of 1-2 cm. A maximum uplift of 6.5 cm is measured at station MOCH further south.

The combined result of the forward poro-viscoelastic model and the afterslip inversion display a lowest mean absolute data error of 5.4 cm (Figure 2a; Table S3), while by neglecting poroelasticity the data misfit slightly increases to 5.5 cm (Figure 2b). Despite this small data fit improvement, our F-test results show that our poro-viscoelastic model is statistically better than a (non-linear) viscoelastic-only model considering a significance level of 0.05 (Figure 2a and Supp. Information). The data fit of the poro-viscoelastic model is 14% better than the one from a pure elastic model (Figure 2c and 2f). In particular, the inclusion of viscoelasticity can substantially improve the data fit in the volcanic and back-arc regions and, to some extent, at the coast (Figure 2d and 2e).

We also show that afterslip processes dominate the near-field deformation (Figure 3a, 3d, and 3g), while non-linear viscoelastic relaxation the surface deformation at volcanic and back arc regions (Figure 3b, 3e, and 3i). The largest poroelastic effects are found close to the region of maximum coseismic slip, while the resulting surface poroelastic response exhibit varying patterns (Figure 3f). Onshore, the poroelastic response exhibits landward and uplift surface deformation, while offshore and particularly close to the trench it is the opposite (Figure 3f). The cumulative poroelastic landward displacements reach up to 0.75 cm, lowering the cumulative displacement of station ILOC by ~15% (Figure 3c and 3h). We also find that the poroelastic response exhibits a maximum coastal uplift of 1.3 cm (Figure 3c and 3f), which is in good agreement with the observations.

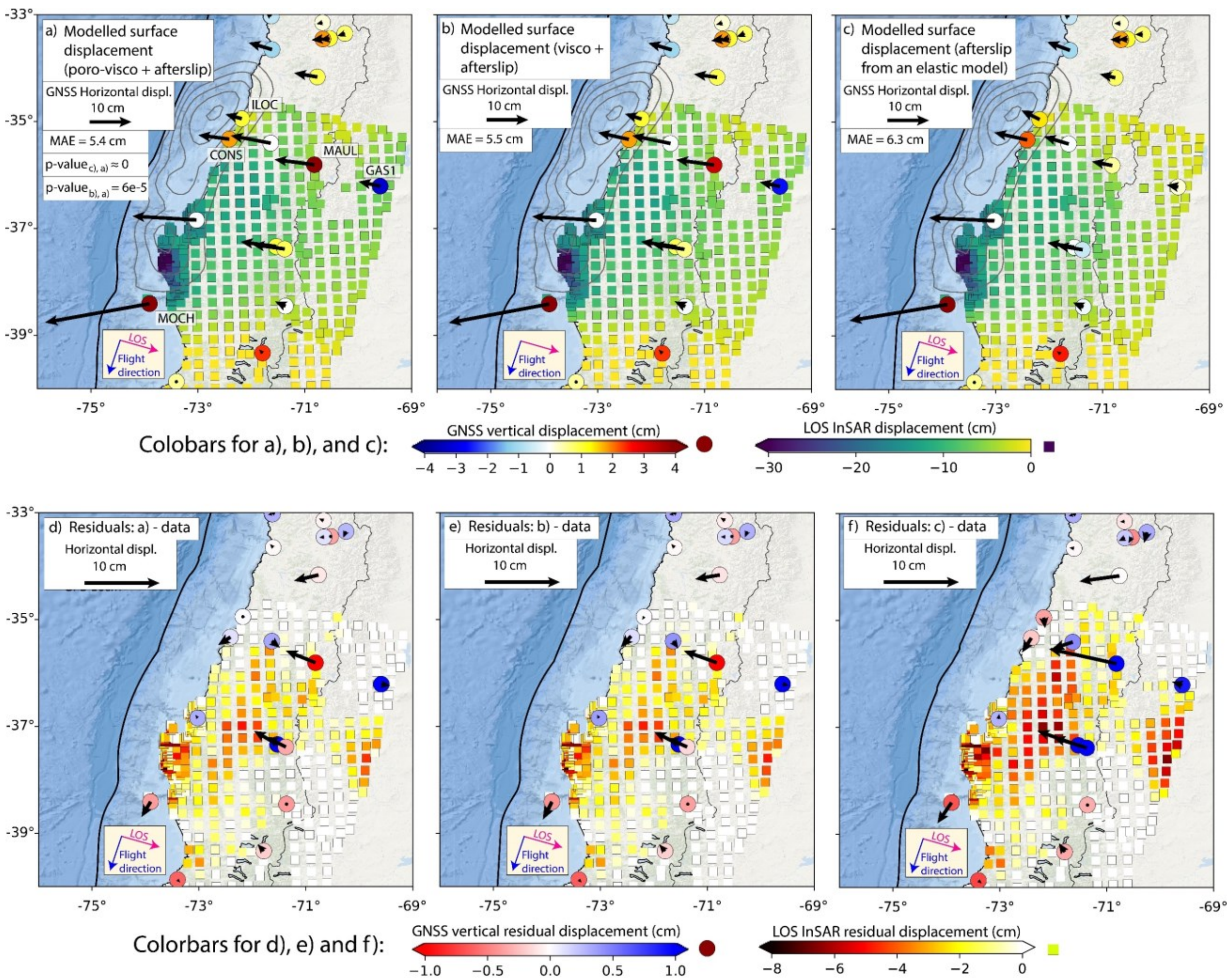

Figure 2. Predicted displacements from forward modelling in combination with an afterslip inversion considering a) poroelasticity and non-linear viscoelasticity, b) non-linear viscoelasticity-only, and c) elasticity-only. MAE represents the mean absolute error. The p-values in a) are obtained by computing the F-values from b) and c) (null hypothesis) with respect to a). d), e) and f) show the residual displacements between the model in a) and c) and the geodetic data.

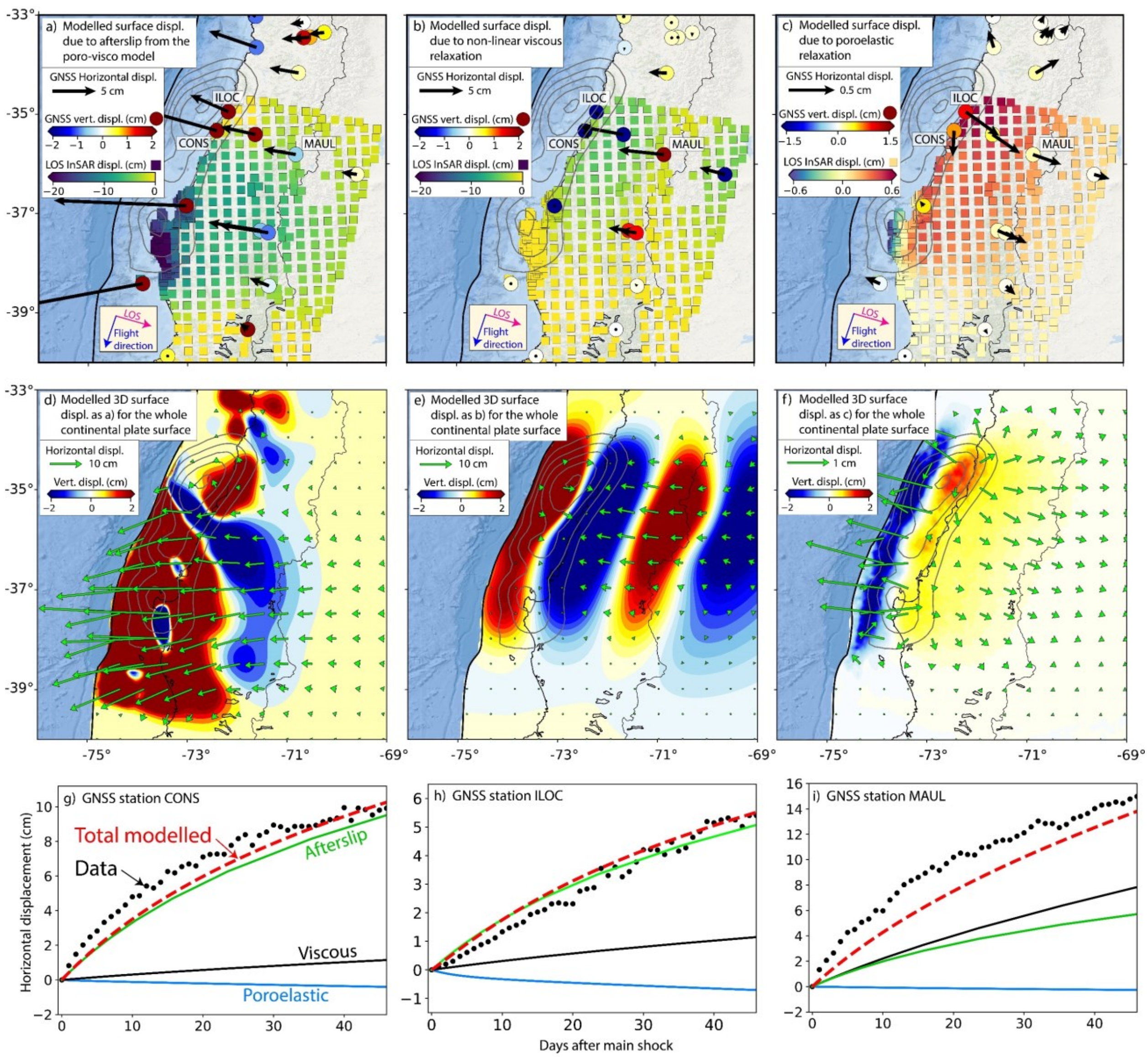

Figure 3. Decomposition of the predicted cumulative and temporal 3D surface displacements from the model that inverts for afterslip considering poro-viscoelasticity. Individual contribution due to a) afterslip, b) viscoelastic, and c) poroelastic processes at the observation sites and d), e), and f) in full 3D-resolution. Individual GNSS horizontal time-series decomposition at stations CONS g), ILOC h) and MAUL i). Temporal evolution of afterslip is modelled with a logarithmic function as $A(t) = A_o \log((t + t_c)/t_r)$, where A_o is the cumulative afterslip calculated from the inversion approach, t is the time after the main shock, t_r is the characteristic time of relaxation, and t_c the critical time, which is introduced to avoid the singularity at $t = 0$ (Avoauc et al., 2015).

5. Spatial distributions of afterslip

We further compare afterslip distributions resulting from a poro-viscoelastic, poroelastic and elastic models. Overall, these models predict most of the afterslip occurring outside regions of high coseismic slip (Figure 4a and 4c), with maximum afterslip amplitude in the southern segment at 37.7°S at 20 km depth. In the northern segment, however, the afterslip predicted by the poro-viscoelastic model differs. It is notably reduced by more than 30 cm close to the trench and by 20-30 cm at 20-50 km depths (Figure 4d). At 20-50 km depth, afterslip resolution and bootstrapping tests report robust results (Figure S4 and S5; Bedford et al., 2013; Peña et al., 2020). We find a general reduction of the afterslip by 16% if poro-viscoelastic effects are incorporated. Viscoelastic effects dominate the prediction as the poroelastic effects (Figure 4e) are significantly smaller than those from the combined model (Figure 4d). However, poroelastic effects alter the afterslip distribution by up to ±25 cm in regions of ~50×50 km^2 (Figure 4e), representing up to ±40% of deviation from the elastic-only model (Figure 4f). These effects are strongest near the region of maximum coseismic slip, where poroelastic effects contribute most to the observed surface displacements (Figure 3c).

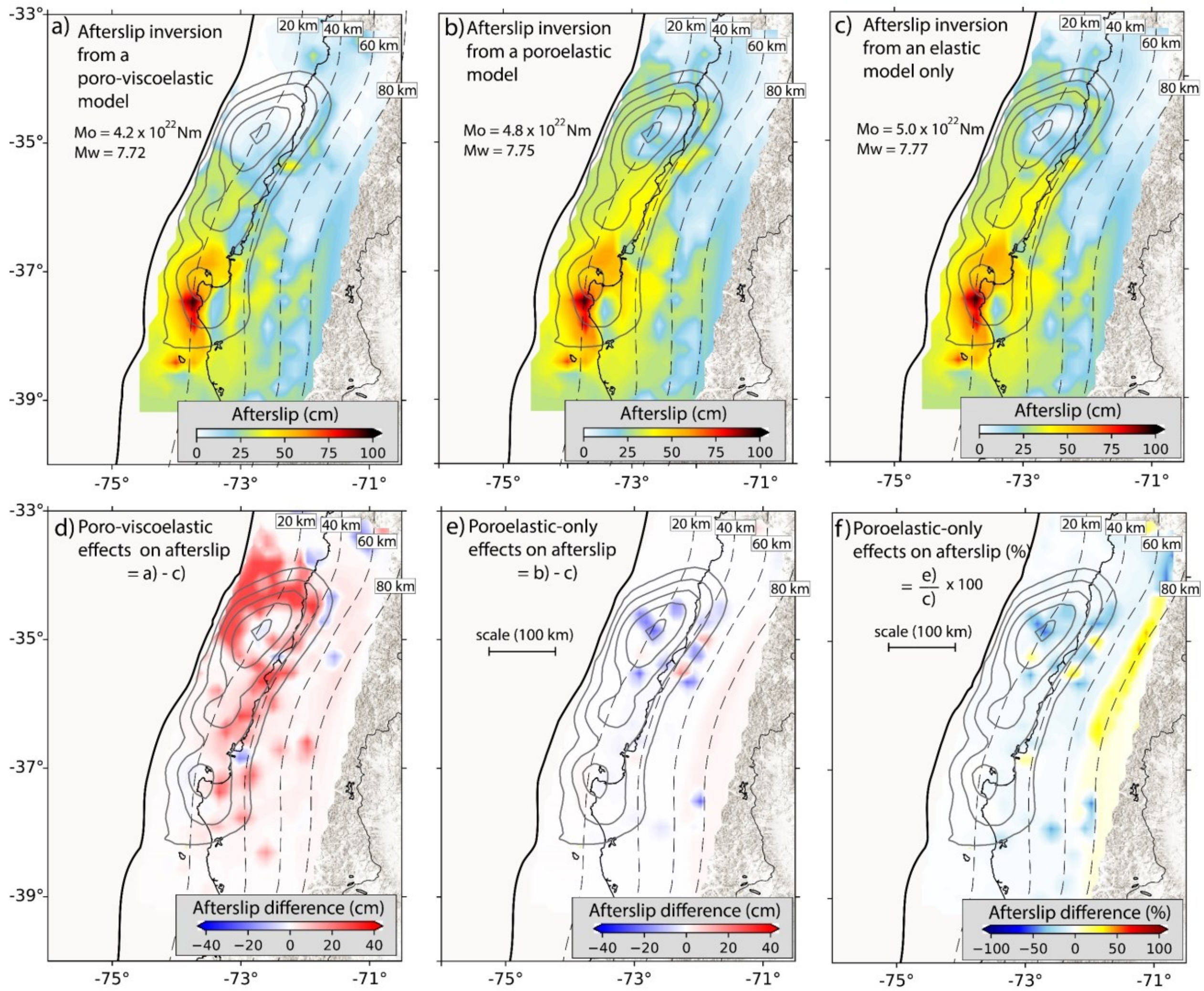

Figure 4. Afterslip distributions from a) the poro-viscoelastic, b) the poroelastic-only and c) the elastic-only models. Grey contour lines show coseismic slip as in Figure 1. Dashed lines represent the plate interface depth from Hayes et al. (2012). d) and e) exhibit afterslip differences between a) and b), and b) and c), respectively, while f) as e) but in percent.

6. Discussion

Poroelastic processes in the upper crust are a fundamental aspect of rock mechanics (e.g., Beeler et al., 2000; Oncken et al., 2021; Warren-Smith et al., 2018). Yet, they have been commonly ignored in postseismic deformation studies. We show that following the Maule event, poroelastic processes affect horizontal GNSS observations by up to 15% (Figure 3c). Moreover, poroelastic processes locally alter the estimated afterslip by up to ±40% near the region of maximum coseismic slip compared to the results of a purely elastic model. Similar patterns have been also reported for the 2012 Nicoya Costa Rica (McCormark et al., 2020) and the 2015 Illapel Chile (Yan et al., 2022) earthquakes. Nonetheless, in the work by McCormark et al. (2020) and Yang et al. (2022) the poroelastic effects on both the geodetic signal and afterslip amplitudes are generally larger than in our study. This might be because these studies neglect viscoelastic relaxation, which also has a significant impact on the afterslip distributions (Figure 4d). In particular, the inclusion of non-linear viscoelasticity considerably reduces the afterslip at shallower segments close to the region of largest coseismic slip (Figure 4a and 4d), thus better explaining the absence of shallow aftershocks (e.g., Lange et al., 2012) (Figure S6).

Our poro-viscoelastic model considers rock parameters that agree with previous studies investigating non-linear viscoelastic (Peña et al., 2020; 2021; Weiss et al., 2019) and poroelastic processes (e.g., Koermer et al., 2004). The permeability of 10^{-14} m^2 used here, however, is about two orders of magnitude higher than that the one used by studies investigating the postseismic deformation of the 2011 Tohoku-Oki (Hu et al., 2014) and the 2004 Sumatra-Andaman megathrust events (Hughes et al., 2010). Nevertheless, these authors either focused on a longer observation period (~2 yrs, Hu et al., 2016) or investigated the stress transfer due to pore-pressure changes (Hughes et al., 2010). This relatively high permeability may be because of upper crustal fractures augmenting permeability locally (e.g., Golima et al., 2016) or a transient response increasing permeability due to the pass of the seismic waves (e.g., Manga et al., 2012), or both processes.

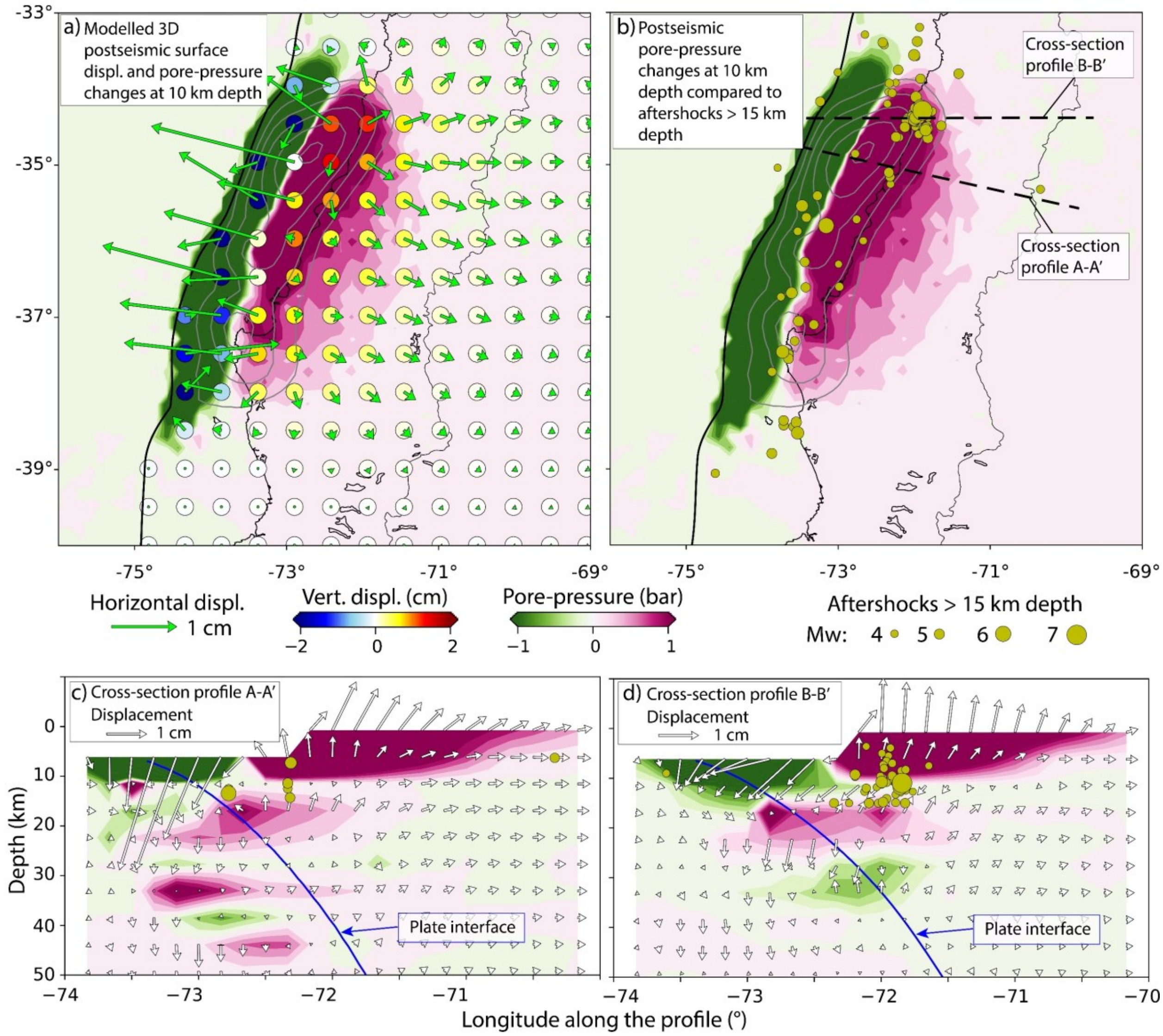

Figure 5. Cumulative postseismic pore-pressure changes, displacement, and $M_{w} \geq 4$ aftershock distribution in the upper 15 km (USGS-NEIC catalogue) during the first 48 days following the main shock.

Our results show that the predicted poroelastic vertical displacement is about two times higher than the horizontal displacement (Figure 3f), which is in good agreement with previous studies (Hu et at., 2014; Hughes et al., 2010; Masterlark et al., 2001; McCormark, et al., 2020). Poroelastic vertical surface displacement patterns can also explain a major part of the observed uplift near the maximum coseismic slip region (Figure 3c). The modelled surface uplift and subsidence pattern is produced by increase and decrease of postseismic pore-pressure changes in the upper crust following the main shock, respectively (Figure 5a and 5c). We also find that shallow aftershocks, especially above ~11 km depth, mostly occur beneath the coastal forearc, where our model predicts pore-pressure increase (Figure 5b-d). An increase of shallow seismic activity following megathrust earthquakes has been observed in many subduction zones (e.g., Soto et al., 2019; Toda et al., 2011), but the mechanisms of these aftershocks are not well understood. Our results indicate that increased postseismic pore-pressure changes may be a plausible triggering process, as they reduce the effective fault normal stress more efficiently than afterslip and viscous processes (e.g., Hughes et al., 2010; Miller et al., 2004).

Given that the vertical surface displacement is highly sensitive to poroelastic effects (Figure 3f), additional geodetic vertical deformation data derived from, for example, offshore pressure gauges (Wallace et al., 2016) or multiple radar look directions (Wright et al., 2004) could be used in future studies to better understand crustal poroelastic processes. Moreover, a homogenous spatial distribution of permeability may not be a realistic representation of the upper crust (e.g., Manga et al., 2012). Additional water-level observations could directly constrain spatial variations of crustal poroelastic properties (McCormark and Hesse, 2018).

7. Conclusion

We use a 4D forward model that considers poroelasticity and non-linear viscoelasticity to invert for the afterslip during the first 48 days of postseismic deformation following the 2010 Maule earthquake. Compared to a purely elastic model inverting for afterslip only, our model approach fits the observed postseismic geodetic data 14% better and yields a reduction of the total predicted afterslip of 16%. The latter is primarily due to the implementation of viscoelasticity. Close to the area of maximum coseismic slip, poroelastic effects play a local, but significant role by dragging the horizontal GNSS observations by up to 15% in the opposite direction and altering the afterslip amplitude by up to ±40% in regions of ~50×50 km^2. Poroelastic effects on postseismic slip budgets may be higher and may play a key role in triggering upper crustal aftershocks. However, additional vertical geodetic and water-level are needed to validate these hypotheses and to improve our knowledge of poroelastic processes in the upper crust.

Acknowledgments

This work has received funding from the Initiative and Networking Fund of the Helmholtz Association through the project “Advanced Earth System Modelling Capacity (ESM)”.

Open Research

GNSS data are available through Bedford et al. (2020). We use the model geometry that is available in Peña et al. (2020). We use Kite software (Isken et al., 2017) from the open-source seismology toolbox Pyrocko (Heimann et al., 2017). The ALOS-2/PALSAR-2 data were provided by the Japanese Aerospace Exploration Agency (JAXA) under the 4th Research Announcement (RA) Program and are available from https://auig2.jaxa.jp/ips/home.

References

Agata, R., Barbot, S.D., Fujita, K., Hyodo, M., Iinuma, T., Nakata, R., Ichimura, T., Hori, T., 2019. Rapid mantle flow with power-law creep explains deformation after the 2011 Tohoku mega-quake. Nat. Commun.10 (1), 1385. https://doi.org/10.1038/s41467-019-08984-7.

Araya Vargas, J., Meqbel, N. M., Ritter, O., Brasse, H., Weckmann, U., Yáñez, G., & Godoy, B. (2019). Fluid distribution in the Central Andes subduction zone imaged with magnetotellurics. Journal of Geophysical Research: Solid Earth, 124, 4017– 4034. https://doi.org/10.1029/2018JB016933

Avouac, J.-P., 2015. From geodetic imaging of seismic and aseismic fault slip to dy-namic modeling of the seismic cycle. Annu. Rev. Earth Planet. Sci.43, 233–271. https://doi.org/10.1146/annurev-earth-060614-105302.

Barbot, S. Frictional and structural controls of seismic super-cycles at the Japan trench. Earth Planets Space 72, 63 (2020). https://doi.org/10.1186/s40623-020-01185-3

Barbot, S., 2018. Asthenosphere flow modulated by megathrust earthquake cycles. Geophys. Res. Lett.45, 6018–6031. https://doi .org /10 .1029 /2018GL078197

Beeler, N. M., Simpson, R. W., Hickman, S. H., and Lockner, D. A. (2000), Pore fluid pressure, apparent friction, and Coulomb failure, J. Geophys. Res., 105(B11), 25533–25542. https://doi.org/10.1029/2000JB900119

Bedford, J. et al. Trajectory models for daily displacement time series in the five years preceding the 2010 Maule Mw 8.8, Chile, and 2011 Tohoku-oki Mw 9.0, Japan earthquakes (GFZ Data Services, 2020); https://doi.org/10.5880/GFZ.4.1.2020.001.

Bedford, J., & Bevis, M. (2018). Greedy automatic signal decomposition and its application to daily GPS time series. Journal of Geophysical Research: Solid Earth, 123, 6992–7003. https://doi.org/10.1029/2017JB014765

Bedford, J., Moreno, M., Li, S., Oncken, O., Baez, J. C., Bevis, M., Heidbach, O., & Lange, D. (2016). Separating rapid relocking, afterslip, and viscoelastic relaxation: An application of the postseismic straightening method to the Maule 2010 cGPS, J. Geophys. Res. Solid Earth, 121, 7618–7638. https://doi.org/10.1002/2016JB013093

Bedford, J., Moreno, M., Baez, J.C., Lange, D., Tilmann, F., Rosenau, M., et al. (2013). A high-resolution, time-variable after slip model for the 2010 Maule Mw = 8.8, Chile megathrust earthquake, Earth Planet. Sci. Lett., 383, 26–36. https://doi.org/10.1016/j.epsl.2013.09.020

Cavalié, O., Pathier, E., Radiguet, M., Vergnolle, M., Cotte, N., Walpersdorf, A., et al. (2013). Slow slip event in the Mexican subduction zone: Evidence of shallower slip in the Guerrero seismic gap for the 2006 event revealed by the joint inversion of InSAR and GPS data. Earth and Planetary Science Letters, 367, 52–60. https://doi.org/10.1016/j.epsl.2013.02.020

Costantini, M., (1998). A novel phase unwrapping method based on network programming, in IEEE Transactions on Geoscience and Remote Sensing, 36(3,) 813-821. http://doi.org/10.1109/36.673674

Gomila, R., Arancibia, G., Mitchell, T. M., Cembrano, J. M., & Faulkner, D. R. (2016). Palaeopermeability structure within fault-damage zones: A snap-shot from microfracture analyses in a strike-slip system. Journal of Structural Geology, 83, 103–120. https://doi.org/10.1016/j.jsg.2015.12.002

Christensen, N., 1996. Poisson's ratio and crustal seismology. J.Geophys. Res.101 (B2), 3139–3156. https://doi.org/10.1029/95JB03446.

Farr, T. G., Rosen, P. A., Caro, E., Crippen, R., Duren, R., Hensley, S., et al. (2007). The shuttle radar topography mission. Review of Geophysics, 45, RG2004. https://doi.org/10.1029/2005RG000183

Goldstein, R.M. & Werner, C.L., 1998. Radar interferogram filtering for geophysical applications, Geophys. Res. Lett., 25(21), 4035–4038. https://doi.org/10.1029/1998GL900033

Guo, R., Zheng, Y., Xu, J., Shahid Riaz, M., (2019). Transient Viscosity and Afterslip of the 2015 Mw 8.3 Illapel, Chile, Earthquake. Bulletin of the Seismological Society of America, 109 (6), 2567–2581. https://doi.org/10.1785/0120190114

Heimann, Sebastian; Kriegerowski, Marius; Isken, Marius; Cesca, Simone; Daout, Simon; Grigoli, Francesco; Juretzek, Carina; Megies, Tobias; Nooshiri, Nima; Steinberg, Andreas; Sudhaus, Henriette; Vasyura-Bathke, Hannes; Willey, Timothy; Dahm, Torsten (2017): Pyrocko - An open-source seismology toolbox and library. GFZ Data Services. https://doi.org/10.5880/GFZ.2.1.2017.001

Hergert, T., & Heidbach, O. (2006). New insights into the mechanism of the postseismic stress relaxation exemplified by the 23 June Mw = 8.4 earthquake in southern Peru, Geophys. Res. Lett., 30, L02307. https://doi.org/10.1029/2005GL024858

Hirth, G., & Kohlstedt, D. (2003). Rheology of the upper mantle and the mantle wedge: A view from the experimentalists. Inside the subduction Factory, 83-105. https://doi.org/10.1029/138GM06

Hu, Y., Bürgmann, R., Freymueller, J., Banerjee, P. and Wang, K. (2014). Contributions of poroelastic rebound and a weak volcanic arc to the postseismic deformation of the 2011 Tohoku earthquake. Earth, Planets and Space, 66(1), 106. https://doi.org/10.1186/1880-5981-66-106

Hughes, K. L., et al. (2010). Poroelastic stress-triggering of the 2005 M8. 7 Nias earthquake by the 2004 M9. 2 Sumatra–Andaman earthquake. Earth and Planetary Science Letters 293(3-4), 289-299. https://doi.org/10.1016/j.epsl.2010.02.043

Husen, S. and Kissling, E. (2001); Postseismic fluid flow after the large subduction earthquake of Antofagasta, Chile. Geology 229 (9): 847–850. https://doi.org/10.1130/0091-7613(2001)029<0847:PFFATL>2.0.CO;2

Ingebritsen, S.E. and Manning, C.E. (2010), Permeability of the continental crust: dynamic variations inferred from seismicity and metamorphism. Geofluids, 10: 193-205. https://doi.org/10.1111/j.1468-8123.2010.00278.x

Isken, Marius; Sudhaus, Henriette; Heimann, Sebastian; Steinberg, Andreas; Daout, Simon; Vasyura-Bathke, Hannes (2017): Kite - Software for Rapid Earthquake Source Optimisation from InSAR Surface Displacement. V. 0.1. GFZ Data Services. https://doi.org/10.5880/GFZ.2.1.2017.002

Jónsson, S., Zebker, H.A., Segall, P. & Amelung, F., (2002). Fault slip distribution of the 1999 Mw7.2 Hector Mine earthquake, California, estimated from satellite radar and GPS measurements, Bull. seism. Soc. Am., 92(4), 1377–1389.doi: https://doi.org/10.1785/0120000922

Klein, E., Fleitout, L., Vigny, C., & Garaud, J. D. (2016). Afterslip and viscoelastic relaxation model inferred from the large-scale postseismic deformation following the 2010 Mw 8.8 Maule earthquake (Chile). Geophysical Journal International, 205(3), 1455–1472. https://doi.org/10.1093/gji/ggw086

Koerner, A., Kissling, E., and Miller, S. A. (2004), A model of deep crustal fluid flow following the Mw = 8.0 Antofagasta, Chile, earthquake, J. Geophys. Res., 109, B06307. https://doi.org/10.1029/2003JB002816

Lange, D., Tilmann, F., Barrientos, S.E., Contreras-Reyes, E., Methe, P., Moreno, M., Heit, B., Agurto, H., Bernard, P., Vilotte, J.-P., Beck, S. (2012). Aftershock seismicity of the 27 February 2010 Mw 8.8 Maule earthquake rupture zone. Earth Planet. Sci. Lett.317–318, 413–425. https://doi .org /10 .1016 /j.epsl .2011.11.034.

Li, S., Bedford, J., Moreno, M., Barnhart, W. D., Rosenau, M., & Oncken, O. (2018). Spatiotemporal variation of mantle viscosity and the presence of cratonic mantle inferred from 8 years of postseismic deformation following the 2010 Maule, Chile, earthquake. Geochemistry, Geophysics, Geosystems, 19, 3272– 3285.

https://doi.org/10.1029/2018GC007645

Li, S., Moreno, M., Bedford, J., Rosenau, M., and Oncken, O. (2015), Revisiting viscoelastic effects on interseismic deformation and locking degree: A case study of the Peru-North Chile subduction zone. J. Geophys. Res. Solid Earth, 120, 4522–4538. http://doi.org/10.1002/2015JB011903

Lin, Y. N., Kositsky, A. P., and Avouac, J.-P. (2010). PCAIM joint inversion of InSAR and ground-based geodetic time series: Application to monitoring magmatic inflation beneath the Long Valley Caldera, Geophys. Res. Lett., 37, L23301, doi:10.1029/2010GL045769.

Liu, S., Shen, Z., Bürgmann, R., Jónsson, S. (2020). Thin crème brûlée rheological structure for the Eastern California Shear Zone. Geology 49 (2): 216–221. https://doi.org/10.1130/G47729.1

Luo, H., Wang, K. (2021). Postseismic geodetic signature of cold forearc mantle in subduction zones. Nat. Geosci. 14, 104–109. https://doi.org/10.1038/s41561-020-00679-9

Manga, M., Beresnev, I., Brodsky, E. E., Elkhoury, J. E., Elsworth, D., Ingebritsen, S. E., Mays, D. C., and Wang, C.-Y. (2012). Changes in permeability caused by transient stresses: Field observations, experiments, and mechanisms, Rev. Geophys., 50, RG2004. https://doi.org/10.1029/2011RG000382

Masterlark, T., DeMets, T. C., and Wang, H. F. (2001). Homogeneous vs heterogeneous subduction zone models: Coseismic and postseismic deformation. Geophysical Research Letters 28(21): 4047-4050. https://doi.org/10.1029/2001GL013612

Masterlark, T., and Wang, H. F. (2002). Transient Stress-Coupling Between the 1992 Landers and 1999 Hector Mine, California, Earthquakes. Bulletin of the Seismological Society of America. 92 (4), 1470–1486. https://doi.org/10.1785/0120000905

Masterlark, T., (2003). Finite element model predictions of static deformation from dislocation sources in a subduction zone: sensitivities to homogeneous, isotropic, Poisson-solid, and half-space assumptions. J.Geophys. Res., Solid Earth108 (B11). https://doi .org /10 .1029 /2002JB002296.

McCormack, K. A., and Hesse, M. A. (2018). Modeling the poroelastic response to megathrust earthquakes: A look at the 2012 Mw 7.6 Costa Rican event. Advances in Water Resources, 114, 236–248. https://doi.org/10.1016/j.advwatres.2018.02.014

McCormack, K., Hesse, M. A., Dixon, T. H., and Malservisi, R. (2020). Modeling the contribution of poroelastic deformation to postseismic geodetic signals. Geophysical Research Letters, 47, e2020GL086945. https://doi.org/10.1029/2020GL086945

Melgar, D., Riquelme, S., Xu, X., Baez, J.C., Geng, J., Moreno, M. (2017). The first since 1960: a large event in the Valdivia segment of the Chilean Subduction Zone, the 2016 M7.6 Melinka earthquake. Earth Planet. Sci. Lett. 474, 68–75. https://doi.org/10.1016/j.epsl.2017.06.026

Miller, S., Collettini, C., Chiaraluce, L. et al. (2004). Aftershocks driven by a high-pressure CO2 source at depth. Nature 427, 724–727. https://doi.org/10.1038/nature02251

Moreno, M., Melnick, D., Rosenau, M., Baez, J., Klotz, J., Oncken, O., al. (2012). Toward understanding tectonic control on the Mw 8.8 2010 Maule Chile earthquake, Earth and Planetary Science Letters, 321–322, 152–165. https://doi.org/10.1016/j.epsl.2012.01.006

Oncken, O., Angiboust, S., Dresen, G. (2021). Slow slip in subduction zones: Reconciling deformation fabrics with instrumental observations and laboratory results. Geosphere. https://doi.org/10.1130/GES02382.1

Peña, C., Heidbach, O., Moreno, M., Melnick, D., and Oncken, O. (2021). Transient Deformation and stress Patterns Induced by the 2010 Maule Earthquake in the Illapel Segment. Front. Earth Sci. 9, 644834. https://doi.org/10.3389/feart.2021.644834

Peña, C., Heidbach, O., Moreno, M., Bedford, J., Ziegler, M., Tassara, A., & Oncken, O. (2020). Impact of power-law rheology on the viscoelastic relaxation pattern and afterslip distribution following the 2010 Mw 8.8 Maule earthquake. Earth and Planetary Science Letters 542, 116292. https://doi.org/10.1016/j.epsl.2020.116292

Peña, C., Heidbach, O., Moreno, M., Bedford, J., Ziegler, M., Tassara, A., & Oncken, O. (2019). Role of Lower Crust in the Postseismic Deformation of the 2010 Maule Earthquake: Insights from a Model with Power-Law Rheology. Pure and Applied Geophysics. https://doi.org/10.1007/s00024-018-02090-3

Perfettini, H., Frank, W. B., Marsan, D., & Bouchon, M. (2018). A model of aftershock migration driven by afterslip. Geophysical Research Letters, 45, 2283– 2293. https://doi.org/10.1002/2017GL076287

Press, W., A. Teukolsky, W. Vetterling, and B. Flannery (2002), Numerical Recipes in C: the Art of Scientific Computing, Cambridge Univ Press, Cambridge, U. K.

Ranalli, G., (1997). Rheology and deep tectonics. Ann. Geofis..XL (3), 671–780. https://doi.org/10.4401/ag-3893.

Rolandone, F., Nocquet, J.-M., Mothes, P. A., Jarrin, P., Vallée, M., Cubas, N., et al. (2018). Areas prone to slow slip events impede earthquake rupture propagation and promote afterslip. Sci. Adv. 4 (1), eaao6596. http://doi.org/10.1126/sciadv.aao6596

Soto, H., Sippl, C., Schurr, B., Kummerow, J., Asch, G., Tilmann, F., et al. (2019). Probing the northern Chile megathrust with seismicity: the 2014 M8.1 iquique earthquake sequence. Journal of Geophysical Research: Solid Earth, 124, 12935–12954. https://doi.org/10.1029/2019JB017794

Sudhaus, H. and Jónsson, S. (2009). Improved source modelling through combined use of InSAR and GPS under consideration of correlated data errors: application to the June 2000 Kleifarvatn earthquake, Iceland. Geophysical Journal International, 176, 389-404. https://doi.org/10.1111/j.1365-246X.2008.03989.x

Sun, T., & Wang, K. (2015). Viscoelastic relaxation following subduction earthquakes and its effects on afterslip determination. Journal of Geophysical Research Solid Earth, 120, 1329–1344. https://doi.org/10.1002/2014JB011707.

Sun, T., Wang, K., Iinuma, T., Hino, R., He, J., Fujimoto, H., Kido, M., Osada, Y., Miura, S., Ohta, Y., Hu, Y. (2014). Prevalence of viscoelastic relaxation after the 2011 Tohoku-oki earthquake. Nature, 514 (7520), 84–87. https://doi.org/10.1038/nature13778.

Tassara, A., Götze, H. J., Schmidt, S., and Hackney, R. (2006). Three-dimensional density model of the Nazca plate and the Andean continental margin. J. Geophys. Res. Solid Earth, 111(B9). https://doi.org/10.1029/2005JB003976

Toda, S., Lin, J. & Stein, R.S. (2011). Using the 2011 Mw 9.0 off the Pacific coast of Tohoku Earthquake to test the Coulomb stress triggering hypothesis and to calculate faults brought closer to failure. Earth Planet Sp., 63, 39. https://doi.org/10.5047/eps.2011.05.010

Tsang, L. L. H., Vergnolle, M., Twardzik, C., Sladen, A., Nocquet, J.-M., Rolandone, F., et al. (2019). Imaging rapid early afterslip of the 2016 Pedernales earthquake, Ecuador. Earth Planet. Sci. Lett. 524, 115724. https://doi.org/10.1016/j.epsl.2019.115724

Tung, S., and Masterlark, T. (2018). Delayed poroelastic triggering of the 2016 October Visso earthquake by the August Amatrice earthquake, Italy. Geophysical Research Letters 45(5), 2221-2229. https://doi.org/10.1002/2017GL076453

Wallace, L. M., Webb, S. C., Ito, Y., Mochizuki, K., Hino, R., Henrys, S., et al. (2016). Slow slip near the trench at the Hikurangi subduction zone, New Zealand. Science, 352(6286), 701–704. https://doi.org/10.1126/science.aaf2349

Wang, H.F., 2000. Theory of Linear Poroelasticity: With Applications to Geomechanics. Princeton University Press, Princeton.

Wang, K., Hu, Y., & He, J. (2012). Deformation cycles of subduction earthquakes in a viscoelastic Earth, Nature, 484(7394), 327–332. https://doi.org/10.1038/nature11032

Warren-Smith, E., Fry, B., Wallace, L. et al. (2019). Episodic stress and fluid pressure cycling in subducting oceanic crust during slow slip. Nat. Geosci. 12, 475–481. https://doi.org/10.1038/s41561-019-0367-x

Weiss, J. R., Walters, R. J., Morishita, Y., Wright, T. J., Lazecky, M., & Wang, H., et al. (2020). High-resolution surface velocities and strain for Anatolia from Sentinel-1 InSAR and GNSS data. Geophysical Research Letters, 47, e2020GL087376. https://doi.org/10.1029/2020GL087376

Weiss, J. R., Qiu, Q., Barbot, S., Wright, T. J., Foster, J. H., Saunders, A., et al. (2019). Illuminating subduction zone rheological properties in the wake of a giant earthquake. Science advances, 5(12), eaax6720. http://doi.org/10.1126/sciadv.aax6720

Wegmüller, U., & Werner, C. (1997). Gamma SAR processor and interferometry software, Proc. of the 3rd ERS Scientific Symposium on space at the service of our environment, 14-21 March 1997, Florence Italy.

Welstead, S. T. (1999), Fractal and Wavelet Image Compression Techniques, 232 pp., SPIE Opt. Eng., Bellingham, Washington.

Werner, C., Wegmüller, U., Frey, O., Santoro, M. (2011). Interferometric processing of PALSAR wide-beam ScanSAR data, Fringe 2011, 8th International Workshop on "Advances in the Science and Applications of SAR Interferometry", 19-23 Sep 2011, Frascati, Italy.

Williamson, A.L., and Newman, A.V., (2018). Limitations of the resolvability of finite-fault models using static land-based geodesy and open-ocean tsunami waveforms. Journal of Geophy. Res., Solid Earth, 123(10), 9033-9048. https://doi.org/10.1029/2018JB016091

Wright, T. J., Parsons, B. E., and Lu, Z. (2004). Toward mapping surface deformation in three dimensions using InSAR, Geophys. Res. Lett., 31, L01607. https://doi.org/10.1029/2003GL018827

Yang, H., Guo, R., Zhou, J., Yang, H., Sun, H. (2022). Transient poroelastic response to megathrust earthquakes: a look at the 2015 Mw 8.3 Illapel, Chile, event. Geophysical Journal International, ggac099, https://doi.org/10.1093/gji/ggac099

Supporting Information for

Role of poroelasticity during the early postseismic deformation of the 2010 Maule megathrust earthquake

Carlos Peña[1,2], Sabrina Metzger[1], Oliver Heidbach[1,3], Jonathan Bedford[1], Bodo Bookhagen[2], Marcos Moreno[4], Onno Oncken[1,5], and Fabrice Cotton[1,2]

[1] Helmholtz Centre Potsdam, GFZ German Research Centre for Geosciences, Potsdam, Germany

[2] Institute of Geosciences, University of Potsdam, Germany

[3] Institute of Applied Geosciences, Technical University Berlin, Germany

[4] Departamento de Geofísica, University of Concepción, Chile

[5] Department of Earth Sciences, Freie Universität Berlin, Berlin, Germany

Corresponding author: carlosp@gfz-potsdam.de

Contents of this file

1.- Geodetic observations

Fig. S1a shows the uncertainty that results both in the GNSS horizontal and vertical component. In the vertical component, the uncertainty represents about 40% of the overall vertical signal. The uncertainty for the horizontal component is much smaller, representing approximately 10% of the total signal only. Before the afterslip inversion, we removed a linear ramp from the InSAR data as explained in the main text using the GNSS data. This approach produces a good agreement between the GNSS displacements, collapsed into line-of-sight, and the InSAR displacements (Figure S1b).

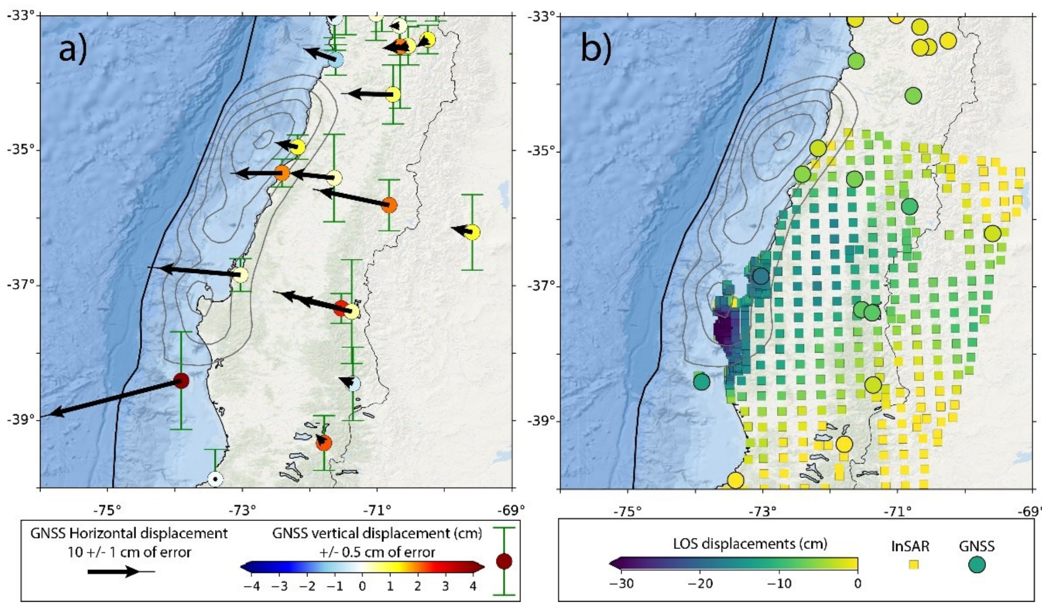

Figure S1. Horizontal and vertical GNSS data uncertainty (a) and deramped InSAR, and GNSS displacements, collapsed into LOS (b).

2.- Model geometry

We use the 4D model geometry of Peña et al. (2020). The model incorporates the slab geometry of Hayes et al. (2012) and the Moho discontinuity from Tassara et al. (2006). It extends 4000 km in West-East, 2000 km in North-South and 400 km in the vertical direction (Fig. 3 in Peña et al., 2020). This is large enough to avoid artefacts due to model boundary conditions. The model volume is discretized into 2,350,000 finite elements with a higher resolution close to the area of expected postseismic deformation (~3 km) and coarser resolution (~50 km) at the model boundaries. To initiate the postseismic deformation we simulate the coseismic rupture of the Maule M_w 8.8 earthquake using the coseismic slip model from Moreno et al. (2012) on a fault that is ~700 km long in strike direction and ~90 km deep. The relative displacement of the hanging and foot walls is governed by linear constraint equations that satisfy the specified slip at each node (Masterlark, 2003).

3.- F-test

We calculate the p-values by first computing the F-values as follows:

$$F = \frac{(S_1^2 - S_2^2) \times df_2}{(df_1 - df_2) \times S_2^2}$$

where S_1^2 and S_2^2 represent the residual sum of the squares of the model of the model with fewer and higher model parameters, respectively, while df_1 and df_2 are the degrees of freedom associated to these modes, respectively, and calculated as N – P, with N representing number of data samples and P the number of model parameters (e.g., Press et al., 2002). We perform two calculations by comparing the model results from 1) the poro-viscoelastic and the elastic-only models and 2) the poro-viscoelastic model and (non-linear) viscoelastic-only model. The latter, in particular, compare to what extend the implementation of poroelasticity is statistically significant given the small geodetic data fit improvement is not conclusive. We thus consider in 1) and 2) as null hypotheses as the elastic-only and viscoelastic-only models, i.e., that the implementation of poro-viscoelasticity and poroelasticity, respectively, does not provide a significant better improvement. We use the python function *scipy.stats.f.sf* to obtain the p-values based on the calculated F-value. For the case 1) we find an F-value = 7.87 and for case 2) an F-value = 1.28, yielding to p-values of 3.27×10^{-129} and 6.6×10^{-4}, respectively. These small values are in good agreement with those resulting from studies considering highly dense geodetic measurements (e.g., Lin et al., 2010). These p-value are considerably smaller than a significance level of 0.05, and therefore the null hypotheses are rejected.

4.- Afterslip inversion

The afterslip inversion is obtained after removing the poroelastic and viscoelastic component to the geodetic data (see main text). We then apply an afterslip inversion approach considering the following constraints: 1) back-slip is not allowed, 2) the rake vector angle is constrained to occur in the up-dip direction between 60° and 120° (this mostly agrees with the rake of aftershocks during the early postseismic deformation, e.g., Lange et al., 2012), and 3) smoothing Laplacian constraints (e.g., Bedford et al., 2013; Peña et al., 2020). We test different relative weighting of the InSAR and GNSS data sets following Cavalié et al. (2013) using the model considering poro-viscoelasticity. Here, we find that a relative weight of 0.6 can best explain both data sets as displayed in Figure S2. To be able to directly compare our results, we use the same relative weight factor for all afterslip inversions, i.e., using a fully elastic and poroelastic model. To reduce computation time to generate the Green's functions, we group nodes within a moving spatial window of 10×10 km^2 along the fault interface (e.g., Li et al., 2015).

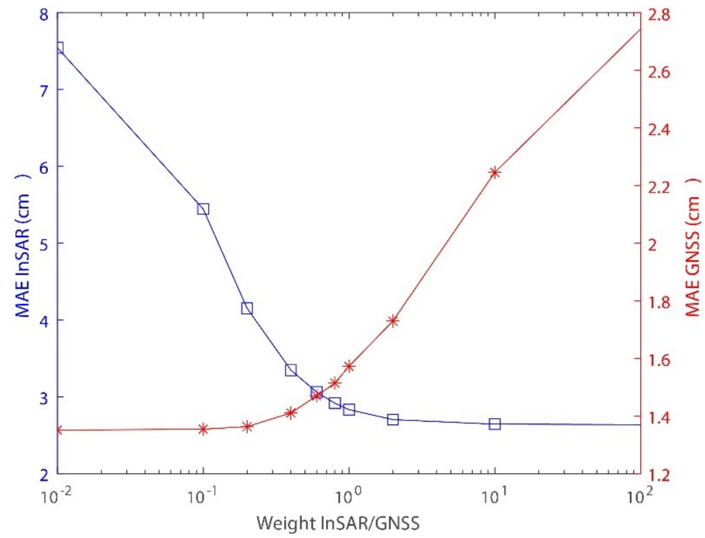

Figure S2. Misfit functions of InSAR and GNSS data using a varying relative weight. MAE means mean absolute error.

5. Coupled versus uncoupled model tests

In the coupled model (Figure S3a), the afterslip distribution obtained after removing the visco-poroelastic effects (Figure 5a in the main text) is implemented as a displacement boundary condition on the model fault interface along with poroelasticity and viscoelasticity through a forward simulation to model the simultaneous surface displacement response to the three postseismic processes investigated in this study. In contrast, the uncoupled model (Figure S3b) is the sum of the individual contributions from each postseismic process to the surface displacement field. Note that the differences in Figure S3c are relatively small and lower than the uncertainty of the GNSS data of approximately 10% in the horizontal and up to 40% in the vertical.

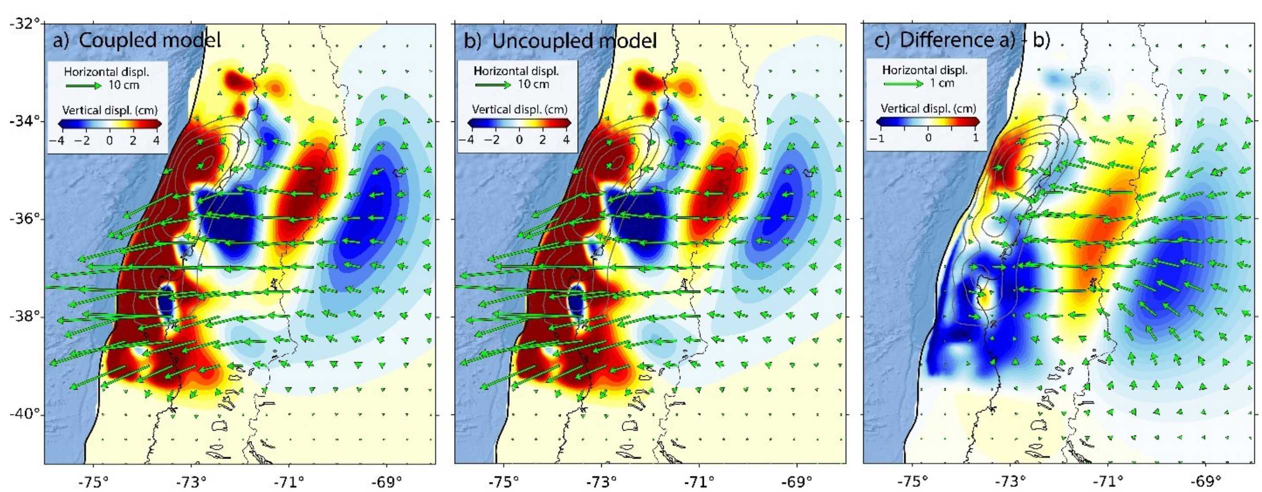

Figure S3. Cumulative 3D surface displacement field from model coupling tests.

6. Afterslip uncertainty and resolution test model

We compute the afterslip standard deviation using bootstrapping tests after randomly removing 10% of the geodetic data with replacement for 200 iterations (e.g., Melgar et al., 2017). At the location of the largesr poroelastic effects (black rectangles in Figure S4) we find that the afterslip differences can reach ±25 cm, which is at least six times larger than the mean afterslip standard deviation resulting from bootstrapping tests (Figure S4c). We also compute the resolution and spread (after)slip model following Williamson and Newman (2018) (Figure S5). The resolution **R** is calculated as $\mathbf{R} = [\, G^T G + \epsilon^2 I \,]^{-1} G^T G$ where G represents the Green's function matrix, I the identity matrix, and ϵ a weighting smoothing parameter. The spread model S is obtained as $\mathbf{S} = L/\sqrt{R}$, with L=10 km as the sub-fault length. The diagonal of **R** provides information about how well afterslip on each fault patch is resolved, given the data kernel and a priori model inputs, ranging from 1 (perfectly resolved) to 0 (unresolved), while **S** the size of the minimum features that can be resolved. In the region where poroelastic processes play a significant role on afterslip distributions (black rectangles in Fig. S4), our model provides a high resolution (> 0.3, Figure 5a), and afterslip patches as small as 10-20 km can be identified (Figure S5c). The tests also show that both the resolution and spread model considerably increase when including InSAR data.

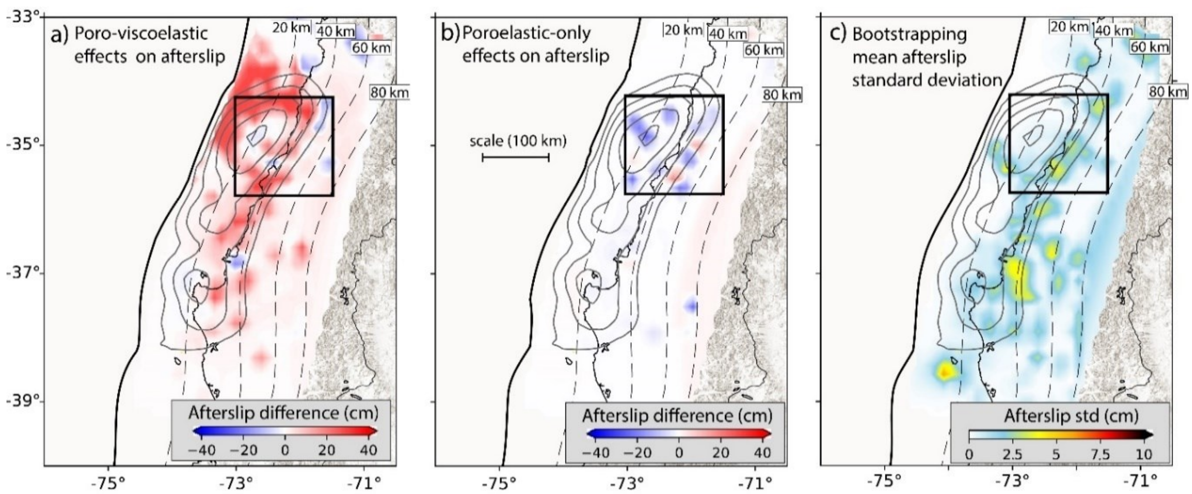

Figure S4. Afterslip uncertainty. Afterslip differences in a) and b) correspond to Fig. 4d and 4e in the main text, respectively.

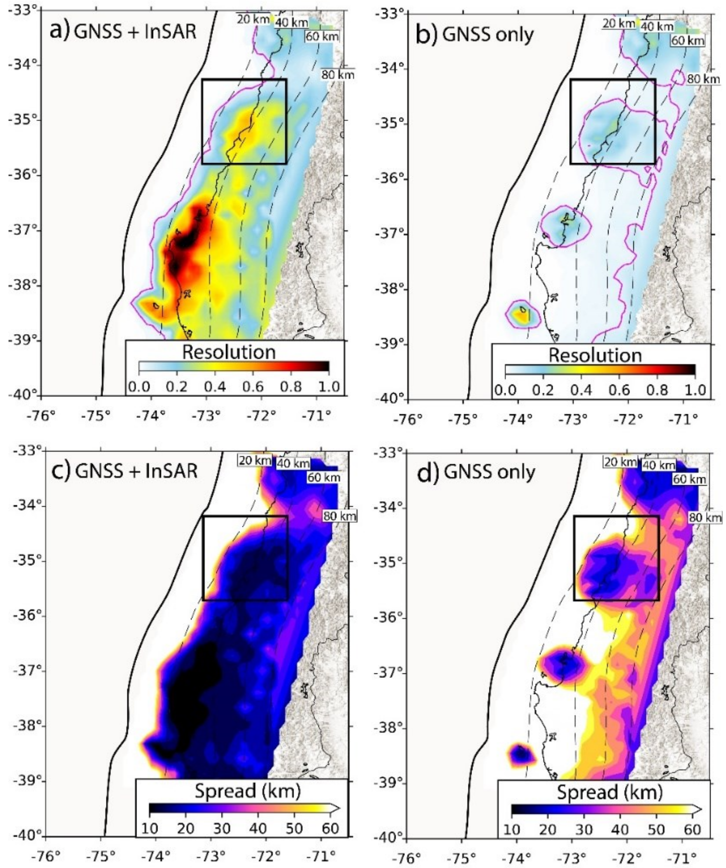

Figure S5. Resolution and spread model tests calculated on the fault interface. Resolution considering GNSS only (a) and GNSS plus InSAR (b). Spread considering GNSS only (c) and GNSS plus InSAR (d). Magenta contour lines in a) and b) exhibit a critical value of 0.1.

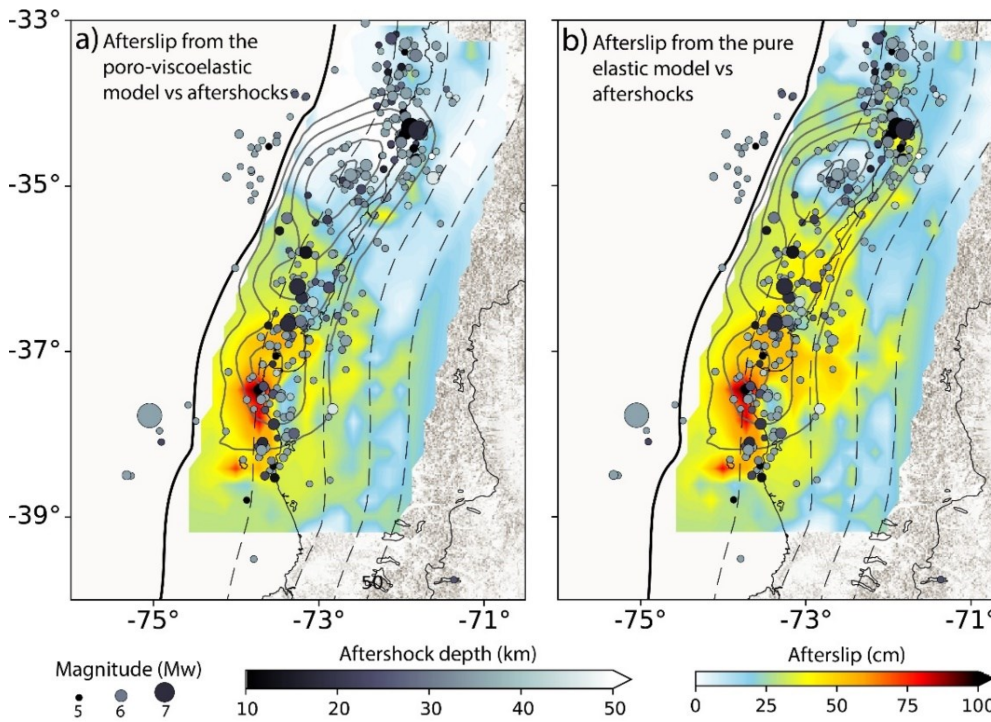

Figure S6. Spatial distribution of modeled afterslip versus observed aftershocks (Mw ≥ 5).

Table S1. Elastic properties and dislocation creep parameters.

Rock type [b]	**Young's modulus E [GPa] [a]**	**Poisson's ratio ν [a]**	**Pre-exponent A [$MPa^{-n}\ s^{-1}$] [b]**	**Stress exponent n [b]**	**Activation energy Q [$kJ\ mol^{-1}$] [b]**
Wet quartzite	100	0.265	3.2×10^{-4}	2.3	154
Wet olivine 1*	160	0.25	5.6×10^{6}	3.5	480
Wet olivine 2*	160	0.25	1.6×10^{5}	3.5	480
Diabase	120	0.3	2.0×10^{-4}	3.4	260

[a] Reference source from Christensen (1996) and Moreno et al. (2012)

[b] Reference source from Hirth and Kohlstedt (2003), Ranalli (1997)

* Wet olivine 1 and 2 contain 0.1 and 0.005% of water, respectively.

Table S2. Poroelastic parameters.

Rock type	Shear modulus E [GPa]	Poison's ration[a]	Permeability [m^2]	Voigt ratio [c]	Porosity [%] [c]
Poroelastic 1	100	0.265	1 x 10^{-14}	0.01	1
Poroelastic 2	100	0.265	1 x 10^{-16}	0.01	1

[c] Reference source from Wang (2000).

Table S3. Simulation configuration. MAE represents the mean absolute error.

Simulation	Continental crust	Continental mantle	Upper crust	MAE [cm]
1	Wet quartzite	Wet olivine 1	Poroelastic 1	5.4
2	Wet quartzite	Wet olivine 1	Poroelastic 2	5.6
3	Wet quartzite	Wet olivine 2	Poroelastic 1	5.7
4	Wet quartzite	Wet olivine 2	Poroelastic 2	5.8
5	Diabase	Wet olivine 1	Poroelastic 1	5.7
6	Diabase	Wet olivine 1	Poroelastic 2	5.9
7	Diabase	Wet olivine 2	Poroelastic 1	6.1
8	Diabase	Wet olivine 2	Poroelastic 2	6.2

References

Bedford, J., Moreno, M., Baez, J.C., Lange, D., Tilmann, F., Rosenau, M., et al. (2013). A high-resolution, time-variable after slip model for the 2010 Maule Mw = 8.8, Chile megathrust earthquake, Earth Planet. Sci. Lett., 383, 26–36. https://doi.org/10.1016/j.epsl.2013.09.020

Christensen, N. (1996). Poisson's ratio and crustal seismology. J. Geophys. Res.101 (B2), 3139–3156. https://doi.org /10.1029/95JB03446.

Hirth, G., & Kohlstedt, D. (2003). Rheology of the upper mantle and the mantle wedge: A view from the experimentalists. Inside the subduction Factory, 83-105. https://doi.org/10.1029/138GM06

Lange, D., Tilmann, F., Barrientos, S.E., Contreras-Reyes, E., Methe, P., Moreno, M., Heit, B., Agurto, H., Bernard, P., Vilotte, J.-P., Beck, S. (2012). Aftershock seismicity of the 27 February 2010 Mw 8.8 Maule earthquake rupture zone. Earth Planet. Sci. Lett.317–318, 413–425. https://doi org /10.1016 /j.epsl .2011.11.034.

Li, S., Moreno, M., Bedford, J., Rosenau, M., and Oncken, O. (2015), Revisiting viscoelastic effects on interseismic deformation and locking degree: A case study of the Peru-North Chile subduction zone. J. Geophys. Res. Solid Earth, 120, 4522– 4538. doi: 10.1002/2015JB011903.

Lin, Y. N., Kositsky, A. P., and Avouac, J.-P. (2010). PCAIM joint inversion of InSAR and ground-based geodetic time series: Application to monitoring magmatic inflation beneath the Long Valley Caldera, Geophys. Res. Lett., 37, L23301, doi:10.1029/2010GL045769.

Masterlark, T. (2003). Finite element model predictions of static deformation from dislocation sources in a subduction zone: sensitivities to homogeneous, isotropic, Poisson-solid, and half-space assumptions. J.Geophys. Res., Solid Earth108 (B11). https://doi .org /10 .1029 /2002JB002296.

Melgar, D., Riquelme, S., Xu, X., Baez, J.C., Geng, J., Moreno, M. (2017). The first since 1960: a large event in the Valdivia segment of the Chilean Subduction Zone, the 2016 M7. 6 Melinka earthquake. Earth Planet. Sci. Lett. 474, 68–75.

Moreno, M., Melnick, D., Rosenau, M., Baez, J., Klotz, J., Oncken, O., al. (2012). Toward understanding tectonic control on the Mw 8.8 2010 Maule Chile earthquake, Earth and Planetary Science Letters, 321–322, 152–165. https://doi.org/10.1016/j.epsl.2012.01.006

Peña, C., Heidbach, O., Moreno, M., Bedford, J., Ziegler, M., Tassara, A., & Oncken, O. (2020). Impact of power-law rheology on the viscoelastic relaxation pattern and afterslip distribution following the 2010 Mw 8.8 Maule earthquake. Earth and Planetary Science Letters 542: 116292.

Press, W., A. Teukolsky, W. Vetterling, and B. Flannery (2002), Numerical Recipes in C: the Art of Scientific Computing, Cambridge Univ Press, Cambridge, U. K.

Ranalli, G. (1997). Rheology and deep tectonics. Ann. Geofis.XL (3), 671–780. https://doi .org /10 .4401 /ag -3893.

Tassara, A., Götze, H. J., Schmidt, S., and Hackney, R. (2006). Three-dimensional density model of the Nazca plate and the Andean continental margin. J. Geophys. Res. Solid Earth, 111(B9). DOI: 10.1029/2005JB003976

Wang, H.F., 2000. Theory of Linear Poroelasticity: With Applications to Geomechanics. Princeton University Press, Princeton.

Williamson, A.L. and Newman, A.V., (2018). Limitations of the resolvability of finite-fault models using static land-based geodesy and open-ocean tsunami waveforms. Journal of Geophy. Res.: Solid Earth, 123(10), pp.9033-9048